Nanoscale

PAPER

Cite this: *Nanoscale*, 2018, **10**, 8704

The phonon confinement effect in two-dimensional nanocrystals of black phosphorus with anisotropic phonon dispersions†

Tong Lin,‡[a,b] Xin Cong,‡[a,b] Miao-Ling Lin,[a,b] Xue-Lu Liu*[a,b] and Ping-Heng Tan *[a,b]

Received 22nd February 2018,
Accepted 29th March 2018

DOI: 10.1039/c8nr01531g

rsc.li/nanoscale

The RWL model for the phonon confinement effect in nanocrystals (NCs) had been found to result in deviations and limitations for crystals exhibiting obvious anisotropic phonon dispersions and modified models have been proposed to overcome these deficiencies. Here, we examine this issue in black phosphorus (BP), a typical anisotropic two-dimensional crystal exhibiting pronounced anisotropy in phonon dispersions. A detailed study is performed on the Raman spectra of BP NCs prepared by the ion implantation technique. With decreasing NC size, the peak positions of the three characteristic Raman modes, A_g^1, B_{2g} and A_g^2 modes, remain almost unchanged, while the A_g^1 and A_g^2 modes show significant asymmetrical broadening tails towards higher- and lower-frequency sides, respectively. It is found that the RWL model based on one-dimensional phonon dispersion along Γ–Y and Γ–X axes in the Brillouin zone (BZ) cannot interpret the unusual frequency invariance and inhomogeneous line shape broadening of these three modes. However, after considering the contribution of two-dimensional anisotropic phonon dispersions from the whole BZ, the frequency and asymmetrical broadening of the A_g^1 and A_g^2 modes can be well reproduced. This study demonstrates that the RWL model can be applicable for crystals with anisotropic phonon dispersions once the phonons in the whole two-dimensional or three-dimensional BZ are properly taken into account, and provides a physically sound route into understanding the phonon confinement effect for anisotropic systems.

1. Introduction

Phonons in a crystal have a strong impact on its physical properties, such as thermal transport, ballistic transport, heat capacity, and carrier dynamics.[1] The fundamental momentum conservation rule of $\mathbf{q} \sim 0$ in the Raman process makes phonons at the Brillouin zone (BZ) center be detectable in pristine bulk crystals. However, this selection rule would be relaxed in nanocrystals (NCs) and phonons of the pristine bulk crystals away from the BZ center could be involved in its Raman scattering process, which is well-known as the phonon confinement effect in NCs.[2,3] The confinement effect of phonons in NCs usually results in peak shift and line shape broadening of Raman peaks, the magnitude of which depends on the size and shape of NCs and also the phonon dispersion curves of the corresponding pristine bulk crystals.[2–7] This provides an approach to probe the phonon dispersion of pristine bulk crystals away from the BZ center, as evidenced in the Raman spectra of two-dimensional (2D) NCs of MoS_2, WS_2 and WSe_2.[8–12]

To better understand the Raman spectra of NCs, a widely-used phonon confinement model with a Gaussian weighting function to demonstrate how fast the phonon amplitude decays to the NC boundary was primitively proposed by Richter, Wang and Ley, which is usually referred to as the RWL model.[2,3] This model has been extensively used to understand the Raman spectra of quantum wells, nanowires, nanoribbons, nanodots and 2D NCs.[2–5,8–16] In order to simplify the calculations, in the RWL model, the phonon dispersion relations are approximately considered to be isotropic in the BZ. At the same time, reliable phonon dispersions are often available only along the high symmetry axes in the BZ. Some previous studies even constructed an analytic expression of monotonically decreased phonon dispersion and/or only considered the phonon contributions from the primary high symmetry axes in the case where the phonon dispersion relation is not experimentally available.[4,5,14,17] This simplified approximation seems to work well in some materials whose optical phonon

[a]State Key Laboratory of Superlattices and Microstructures, Institute of Semiconductors, Chinese Academy of Sciences, Beijing 100083, China. E-mail: liuxuelu@semi.ac.cn, phtan@semi.ac.cn
[b]CAS Center of Excellence in Topological Quantum Computation, and College of Materials Science and Opto-Electronic Technology, University of Chinese Academy of Science, Beijing 100049, China

†Electronic supplementary information (ESI) available. See DOI: 10.1039/C8NR01531G

‡These authors contributed equally to this work.

branch monotonically decreases from the zone center to the edge.[13,18] However, this simplified approximation may yield distorted results in some systems whose phonon dispersion curves are anisotropic along the different high symmetry directions, such as Si nanowires, nano-diamonds and nano-thorium oxides.[14,19–21] Some modified models with different weighting functions have been tried to access a reasonable simulation of the experimental Raman spectra but still leave much to be improved.[6,7,19,21] Therefore, it is crucial to find a material with pronounced anisotropic phonon dispersions to re-examine whether the RWL model is universally applicable for these anisotropic systems.

Abundant 2D crystals provide versatile media to study the phonon physics.[8,22] Some of the 2D crystals, such as graphene and transition metal dichalcogenides, exhibit isotropic properties within the *ab* plane because of the D_{6h} symmetry.[8,22] In contrast, BP is a typically anisotropic 2D crystal with the hinge-like puckered atomic configuration. This structure results in many novel and anisotropic properties. For example, the electronic band dispersions of BP are nearly linear in the armchair direction while quadratic in zigzag directions, giving rise to strong anisotropy in its electronic properties.[23] Furthermore, its phonon dispersion also exhibits in-plane anisotropy.[24] These in-plane anisotropies actually come from the nature of D_{2h} symmetry and its anisotropic Raman response varied with crystallographic directions has been intensely studied,[25–28] which provides a platform to reveal the behavior of anisotropic phonon dispersion on the Raman spectra of NCs addressed above.

The ion-implantation technique has been widely used to gradually introduce defects into 2D crystals to artificially produce the corresponding NCs with different sizes.[29–32] In this work, we report the Raman spectra of the optical phonon modes in BP NCs produced by the ion-implantation technique. With decreasing NC size, the peak position of the three typical Raman modes of BP NCs remains almost unchanged while their bandwidth is asymmetrically broadened. This observed behavior cannot be explained by the RWL model just by considering the phonon dispersion of BP along high symmetry directions. After considering the total contributions from anisotropic phonon dispersion in the whole BZ, the RWL model can well interpret the evolution of the line shape and peak position of BP NCs with decreasing NC size, including a unique asymmetric broadening of the A_g^1 mode towards the higher frequency side and that of the A_g^2 mode towards the lower frequency side. The contributions from the saddle point of the vibrational density of states (VDOS) along high symmetry axes are also essential to explain the line shape broadening of the Raman modes in BP NCs.

2. Experiments and methods

Thin flakes of BPs are prepared from their bulk crystals using the mechanical exfoliation method onto the silicon substrates capped with a 90 nm thick SiO_2 layer. To artificially introduce small-sized NCs, we performed the P^+ implantation experiment with an LC-4 type vacuum system in this work. The kinetic energy of P^+ ions is 100 keV. The samples are subjected to six different ion dosages (η_{ion}), 1×10^{12}, 5×10^{12}, 1×10^{13}, 2×10^{13}, 5×10^{13} and 1×10^{14} cm^{-2}, respectively. The corresponding samples are denoted as #*n*-NC for P^+ ion-implanted BP, where n = 1, 2, 3, 4, 5, 6. The line shapes and peak positions of the Raman spectra of exfoliated thin BP flakes undergo changes in air, due to the introduction of defects or degradation.[33,34] However, the bulk BP with hundreds of nanometer thickness is employed and our Raman measurements are performed immediately after the ion implantation. In the period of Raman measurements, the degradation effect on the Raman spectra can be ignored for the implanted bulk BP.

The phonon dispersion curves of bulk BP are calculated by using the Vienna *ab initio* simulation package (VASP) based on density functional theory (DFT).[35–37] The electron–ion interaction is described by the Projector Augmented Wave (PAW) pseudopotentials. The exchange–correlation function is described by the Perdew, Burke, and Ernzerhof (PBE) version of the generalized gradient approximation (GGA).[38–40] A plane-wave basis set with an energy cut-off of 500 eV was used in our calculations. The conjugated gradient method was proposed in the geometry optimization. The convergence condition for the energy is 10^{-8} eV and the structure was relaxed until the force on each atom was less than 10^{-6} eV $Å^{-1}$. All atoms are relaxed within the Monkhorst–Pack special *k*-point meshes of $7 \times 7 \times 9$. For vibration properties, the Phonopy software[41] is firstly used to determine the atomic displacements, which is necessary to construct the dynamical matrix. Then, we use a supercell of $3 \times 3 \times 4$ and *k*-point meshes of $4 \times 4 \times 4$ to calculate forces by VASP. Finally, the forces are used to calculate phonon dispersion by Phonopy software.

Raman measurements are performed under backscattering configuration at room temperature and under atmospheric pressure using a confocal micro-Raman system (HORIBA Jobin–Yvon HR800) equipped with a liquid nitrogen cooled charge coupled device (CCD). A 1800 lines per mm grating is used, which enables us to have a resolution of 0.60 cm^{-1} per CCD pixel. The excitation wavelength is 488 nm from an Ar^+ laser. The laser is focused onto a spot of approximately 1 μm in diameter with a 100× objective (NA = 0.9). A power of ~0.02 mW is used to avoid line shape changes of Raman modes caused by laser heating.[30]

3. Results and discussion

As the most stable allotropic form of phosphorus, BP was synthesized more than a century ago.[42] Individual puckered layers of phosphorus atoms in BP are stacking together *via* weak van der Waals interactions similar to graphite. Fig. 1(a)–(c) illustrate the BP crystal structure from three different perspectives, where the *x* and *y* axes are the armchair and zigzag directions, and the *z* axis is orthogonal to the P atom layer, respectively. According to the group theory, bulk BP belongs to the point

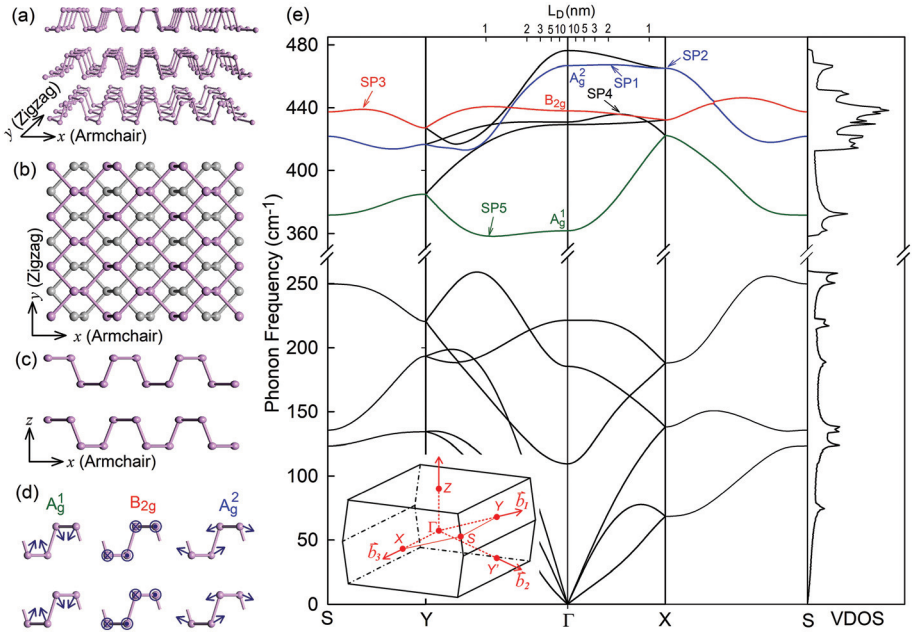

Fig. 1 Structure and phonon dispersions of black phosphorus (BP). (a) Front view of BP with stacking of puckered layers. (b) Top view of BP. The *x* and *y* axes are the armchair and zigzag directions, respectively. (c) Front view of BP. The *z* axis is orthogonal to the P atom layer. (d) Schematic of the atomic displacements for the three typical Raman modes A_g^1, B_{2g}, and A_g^2 in BP. Blue arrows indicate the direction of atomic displacements. (e) Phonon dispersion relations of BP along the high symmetry axes (*S*–*Y*–*Γ*–*X*–*S*) and its corresponding vibrational density of states (VDOS). The inset shows the high symmetry points in the BZ.

group D_{2h}^{18}.[43,44] The unit cell of bulk BP contains 4 atoms, which results in 12 vibrational modes at *Γ*:[43] $\Gamma = 2A_g + B_{1g} + B_{2g} + 2B_{3g} + A_{1u} + 2B_{1u} + 2B_{2u} + B_{3u}$. Among these modes, A_g, B_{1g}, B_{2g} and B_{3g} modes are Raman-active and only three characteristic high-frequency modes A_g^1, B_{2g} and A_g^2 can be observed by Raman scattering under the backscattering geometry. The atomic displacements of these modes are schematically shown in Fig. 1(d). For A_g^2, B_{2g} and A_g^1 modes, atoms move along *x*, *y* and *z* axes, respectively.

We follow the conventional definition of the unit cell of BP (Fig. S1(a)†) and its first BZ (inset of Fig. 1(e)), where $\vec{b}_1$, $\vec{b}_2$ and $\vec{b}_3$ are the reciprocal lattice vectors. The phonon dispersion of bulk BP along the high symmetry axes (*S*–*Y*–*Γ*–*X*–*S*) calculated by DFT is shown in Fig. 1(e). The inset shows the high symmetry points of BP in the first BZ. Since the absolute Raman shifts slightly mismatch with DFT results, the calculated phonon frequencies are shifted by within 0.5% to allow better comparison with the experimental results. BP has three acoustic phonon branches and nine optical phonon branches. These branches are separated into two parts. The high energy part (>300 cm^{-1}) consists of six optical branches while the low energy part (<300 cm^{-1}) has three optical branches and three acoustic branches. It is important to highlight that phonon dispersions of BP show evident differences in the BZ along the *Γ*–*Y* and *Γ*–*X* directions. The phonon branch associated with A_g^2 has a steep and negative dispersion away from *Γ* in the *Γ*–*Y* direction and a nearly flat dispersion in the *Γ*–*X* direction. In contrast, the branch associated with A_g^1 has a nearly flat dispersion in the *Γ*–*Y* direction and a steep and positive dispersion away from *Γ* in the *Γ*–*X* direction. The phonon branch associated with B_{2g} has a slight upward curvature in the *Γ*–*Y* direction near *Γ* and a slight downward curvature in the *Γ*–*X* direction. As for the acoustic phonon modes, the phonon bands are more dispersive along the *Γ*–*Y* direction than the *Γ*–*X* direction. Such anisotropy in phonon dispersion results in the anisotropic physical properties in BP. For example, the anisotropic in-plane thermal conductivities are observed with a larger value in the *Γ*–*Y* direction than in the *Γ*–*X* direction both theoretically and experimentally because of the significant differences in their acoustic phonon bandwidths and group velocities.[45,46]

Fig. 2 depicts the representative Raman spectra of pristine BP and BP implanted by different η_{ion}. The ion-implanted sample can be treated as a crystal with many point defects,[47] which can activate additional Raman peaks by the defect-induced selection rule relaxation in the Raman scattering.[8–12] Alternatively, the ion-implanted sample can also be treated as an ensemble of (circular) NCs. To avoid the temperature influence on frequencies of investigated modes,[48] all Raman spectra were obtained at room temperature with low laser power. The higher η_{ion} of ion-implantation, the smaller size of BP NCs is produced. The prominent features are the three Raman-active $\mathbf{q} \sim 0$ phonon modes at 362.3 cm^{-1} (A_g^1), 436.9 cm^{-1} (B_{2g}) and 466.8 cm^{-1} (A_g^2), which are consistent with previous reports.[43,49] As the size of BP NCs decreases with increasing η_{ion} from 0 (pristine BP) to 1×10^{14} cm^{-2} (#6-NC), the Raman intensities of A_g^1, B_{2g} and A_g^2 modes experience a monotonous decrease. This reflects the worse crystal quality

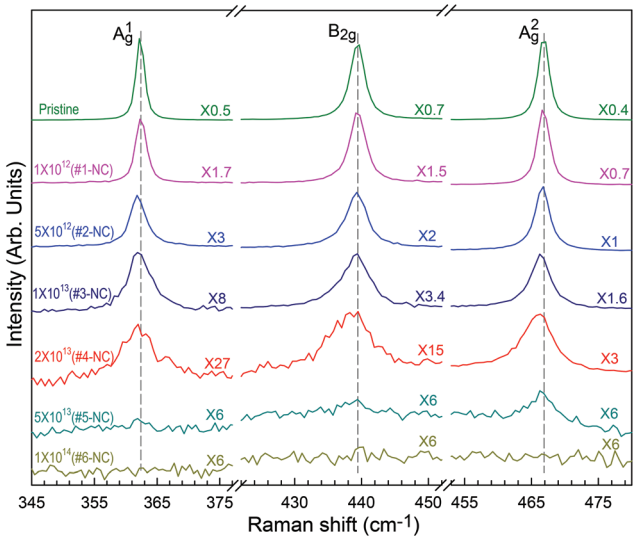

Fig. 2 Raman spectra of pristine BP and BP NCs produced by the ion implantation technique with different η_{ion}. The grey dashed lines are guide to the eye. The excitation wavelength is 488 nm. The Raman intensity is normalized for comparison.

induced by ion-implantation compared with pristine BP, leading to NCs in the implanted samples. This is a common phenomenon in various NCs, such as silicon nanocrystals, nano-diamonds and ion-implanted graphites.[21,29,31,50] Recently several studies on 2D crystals such as transition metal dichalcogenides (TMDs) have also verified a similar downward trend in Raman intensity with increasing η_{ion}.[8,9,11,12] When the pristine BP is subjected to an even higher ion-implantation η_{ion}, such as 5×10^{13} cm^{-2} (#5-NC) and 1×10^{14} cm^{-2} (#6-NC), the Raman modes almost vanish hence becoming too weak and broad to be distinguished, indicating its full amorphization.

In contrast to the significant peak shift of optical modes in Si crystals and other 2D crystals with increasing η_{ion}, the peak shift of the three Raman modes in BP NCs presents a slight redshift with the increment of η_{ion}, as indicated by the grey dashed lines. Raman modes of BPs also exhibit asymmetric broadening after ion-implantation. With increasing η_{ion}, the full width at half maximum (FWHM) evolves from 1.5 cm^{-1} (A_g^1), 2.5 cm^{-1} (B_{2g}) and 1.9 cm^{-1} (A_g^2) in pristine BP into about 4.5 cm^{-1} (A_g^1), 6.0 cm^{-1} (B_{2g}) and 5.2 cm^{-1} (A_g^2) in #4-NC, respectively. Generally, the asymmetric broadening of a Raman peak in NCs towards the higher- or lower-frequency side is often accompanied by the blueshift or redshift of the peak, respectively, as reported in many nanomaterials.[8,11,12,51] Indeed, as shown in Fig. 2, the B_{2g} and A_g^2 modes exhibit asymmetric broadening towards the lower-frequency side. However, the A_g^1 mode shows an asymmetric tail towards the higher-frequency side while its peak position shifts towards the lower-frequency side. The above unusual behavior may be related to the anisotropic phonon dispersion in BPs.

In general, NCs induced by ion implantation can localize the phonon wave function within a finite volume and thus make the fundamental $\mathbf{q} \sim 0$ Raman selection rule to be relaxed, causing the Raman spectrum to have contributions from the non-center phonons. This phonon uncertainty in NCs can be taken into account in the Raman process by a phonon weighting function $W(\mathbf{r}, L_D)$. A Gaussian-type profile of $W(\mathbf{r}, L_D)$ has been widely used in NCs as follows:[3]

$$W(\mathbf{r}, L_D) = \exp(-\alpha r^2/{L_D}^2), \quad (1)$$

where L_D is the domain size of NCs (*i.e.* average inter-defect distance) as illustrated by the previous work,[47] and α is an adjustable confinement coefficient to determine how fast the phonon amplitude decays to the NC boundary. It is noteworthy that since the phonon uncertainty of $\delta\mathbf{q}$ is mainly determined by L_D thus the phonon confinement should affect all the Raman modes in the same manner. Therefore, the same α should be applied to fit the profile of the corresponding Raman modes in the same kinds of NCs with different sizes and symmetries.[11,12] In order to quantitatively analyze the peak shift and asymmetrical broadening of Raman peaks in NCs, the RWL model has been proposed based on $W(\mathbf{r}, L_D)$. The corresponding Raman intensity in the RWL model is given by

$$I(\omega) \propto A(n(\omega)+1)\int \frac{\exp(-q^2{L_D}^2/2\alpha)}{(\omega-\omega(\mathbf{q}))^2+(\Gamma_0/2)^2}\mathrm{d}^3\mathbf{q}, \quad (2)$$

where $n(\omega) + 1$ is the Bose–Einstein factor, which can be treated as a constant for the Raman experiment at room temperature,[50] A is a constant, $\exp(-q^2{L_D}^2/2\alpha)$ is a Fourier coefficient of the Gaussian-type profile $W(\mathbf{r}, L_D)$ in eqn (1), $\omega(\mathbf{q})$ is the phonon dispersion curve, and Γ_0 is the natural broadening. In pristine bulk crystals, L_D can be viewed as infinity and eqn (2) is reduced to a Lorentzian profile centered at ω_0 at the BZ center, with an intrinsic FWHM of Γ_0. As an assumption of isotropic phonon dispersion of $\omega(\mathbf{q})$, the integration can be simplified. For example, in the case of a nanodot, $\mathrm{d}^3\mathbf{q} \propto q^2\mathrm{d}q$, while for a nanowire with length $\gg$ diameter, $\mathrm{d}^3\mathbf{q} \propto q\mathrm{d}q$. For 2D NCs with a diameter of L_D produced from 2D crystals by ion implantation, $\mathrm{d}^3\mathbf{q} \propto 2\pi q\mathrm{d}q$. These integrations have been used for various NCs once the isotropic $\omega(\mathbf{q})$ is assumed for their bulk counterpart.[2,3] This RWL model has been successfully applied to explain the peak shift and broadening in the Raman spectra of many ion-implanted crystals.[8,9,11,12,31,47]

Phonon dispersion is more or less anisotropic in the BZ. For example, phonon dispersion of the LO, TO and ZO branches in MoS_2 shows discrepancy along Γ–M and Γ–K axes.[11,52] Considering that the phonon dispersion along high-symmetry axes can be easily obtained from the published literature, the averaged dispersion curves of each phonon branch between high-symmetry directions of Γ–M and Γ–K are utilized to minimize the anisotropic effect on the experimental results.[11] In contrast to MoS_2 and other TMDs, BP exhibits significant anisotropic phonon dispersion curves, as depicted in Fig. 1(e). The optical phonon dispersion relations along Γ–X and Γ–Y directions behave very differently from each other, so that neither isotropy hypothesis nor average approximation is

a good choice to simulate the Raman spectra based on the RWL model for BP NCs. We first adopted a simple situation by only considering the contributions from one phonon branch along two different high symmetry directions (Γ–X and Γ–Y) in the BZ. The relative contributions from Γ–X and Γ–Y directions to the peak shift and broadening are expected to be the same. The confinement coefficient α is set as 18, similar to that in MoS_2 NCs.[11] Fig. 3 presents the calculated profiles of A_g^1, B_{2g} and A_g^2 modes in implanted samples with different domain size L_D by the RWL model (blue dashed line) compared with the experimental Raman spectra (colored crosshairs). One can see that for pristine BP and BP NCs with larger L_D (#1-NC), the simulated profile has a Lorentzian line shape because the phonon confinement effect can be ignored. Notably, for small L_D (#3-NC and #4-NC), the A_g^1 mode exhibits an asymmetric broadening tail towards the higher-frequency side while the A_g^2 mode towards the lower-frequency side. The above broadening is consistent with the upward trend of the A_g^1 phonon branch along the Γ–X direction and the downward trend of the A_g^2 phonon branch along the Γ–Y direction. Therefore, as the NC size reaches small L_D (#3-NC and #4-NC), the phonon branch with steeper dispersion would contribute greater to the asymmetric broadening of Raman modes while the phonon branch with a dispersionless relation should dominate the peak position.

However, we notice that the experimental data and calculated profiles by the RWL model do not match well for all three phonons of samples with smaller NC sizes which are implanted by higher η_{ion}. The experimental line shapes for the phonon modes are much asymmetrically broader compared to the calculated profiles when the crystal size is smaller than 4.4 nm (#3 NC). Even when the L_D is decreased to as small as 1.8 nm as in #4-NC, where the asymmetric broadening should be the largest, the simulated profiles are much narrower than the experimental results. Some additional peaks of $\mathbf{q} \neq 0$ phonons associated with the saddle point (SP) peaks in VDOS should be involved in the fitting to the experimental data, which are denoted as SP1, SP2, SP3, SP4 and SP5 based on the calculated results, whose origins are indicated in the phonon dispersion curves by arrows in Fig. 1(e). These peaks can be activated by the defect-induced selection rule relaxation in the Raman scattering from NCs, as reported in other 2D materials.[8–12] Although the defect-induced peaks are considered, the experimental data still cannot be well interpreted. For example, the high-frequency tail of the A_g^1 mode and the low-frequency tail of the A_g^2 mode cannot be perfectly reproduced, as indicated with black arrows in Fig. 3. This demonstrates that the consideration of defect-induced peaks and phonon confinement effect only from the Γ–X and Γ–Y directions are not enough to reproduce the experimental results of 2D materials with significant anisotropy. Thus, to understand the Raman spectra of the corresponding NCs, it is necessary to consider phonon dispersion curves in the whole BZ although in most cases they are not available in the reported literature. For the anisotropic crystal like BP, $d^3\mathbf{q}$ in eqn (2) should be $dq_x dq_y dq_z$ and the integration of phonon dispersion in the RWL model over wavevector ($\mathbf{q}$) should cover the whole BZ.

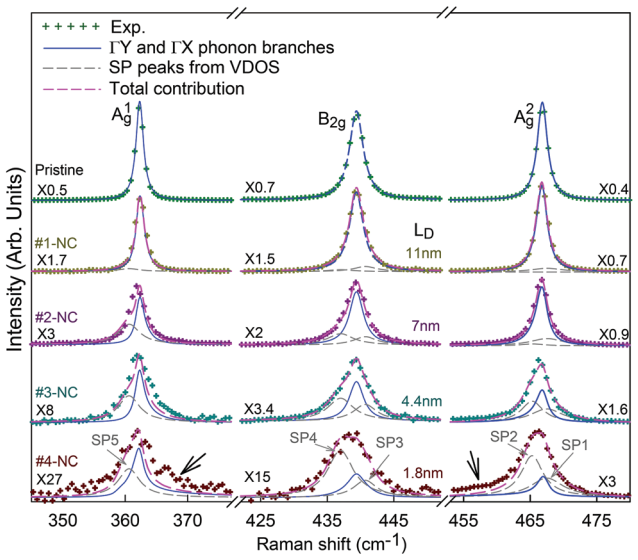

Fig. 3 The experimental data (crosshairs) of the typical Raman modes in pristine BP and BP NC with different estimated domain sizes. The blue dashed lines are the calculated curves only considering the contributions from phonon dispersions along Γ–X and Γ–Y axes. The gray dashed lines are fits based on the SP peaks in the VDOS. The Raman intensity is normalized for comparison.

The phonon dispersion curves in the whole BZ zone of bulk BP are calculated by DFT. We found that phonon dispersions along $\vec{b}_1$ and $\vec{b}_2$ axes are absolutely the same (Fig. S1(b)†). Therefore, it is concluded that $\vec{b}_1$ and $\vec{b}_2$ are equivalent vectors, and phonon dispersion should be the same in the Γ–X–Y and Γ–X–Y' planes. Furthermore, A_g^1, B_{2g} and A_g^2 related phonon branches show little dispersion along the Γ–Z direction (Fig. S1(b)†). So, phonon dispersion in the whole BZ of BP is simplified to that in the Γ–X–Y plane, and the integration of phonon dispersion in the RWL model (eqn (2)) over $d^3\mathbf{q}$ can be reduced to $dq_x dq_y$. Indeed, in the high frequency region above 300 cm^{-1}, the VDOS of the Γ–X–Y 2D plane and the whole BZ show identical features (Fig. S1(b)†), further confirming that the integration of phonon dispersion along dq_z is unnecessary to reproduce the unique line broadening in the concerned frequency region. We further calculated phonon dispersion in the plane enclosed by S–Y–Γ–X–S axes with the 201 × 291 × 1 grid. Its phonon branches related to the A_g^1, B_{2g} and A_g^2 modes are presented in Fig. 4(a) and (b), in which the phonon dispersion related to A_g^1 and A_g^2 experiences high anisotropy from the Γ–Y direction to the Γ–X direction. Based on 2D phonon dispersion obtained by the density grid, we recalculated the Raman profiles of these modes in BP NCs by the RWL model as a function of some specific L_D, as shown in Fig. 4(c). The simulated intensity increases dramatically as the L_D decreases, which is the result of the relaxation of the $\mathbf{q} \sim 0$ selection rule and thus more and more $\mathbf{q} \neq 0$ phonons are involved in the Raman scattering. In principle, the integration over wavevector $\mathbf{q}$ can be accomplished within the whole Γ–Y–S–X plane of BZ using eqn (2). Because the Gaussian-type profile

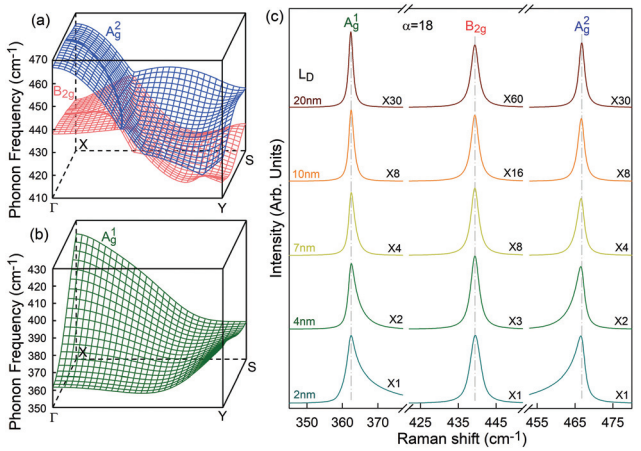

Fig. 4 (a) Phonon dispersion plot of the A_g^2-(blue) and B_{2g}-(light red) related phonon branches and (b) that of the A_g^1-related phonon branch (dark green) in the ΓYSX plane in the first BZ. (c) Simulated profiles of the A_g^1, B_{2g} and A_g^2 modes as a function of L_D with a fixed α = 18. The Raman intensity is normalized for comparison.

$\exp(-q^2L_D^2/2\alpha)$ in eqn (2) demonstrates the phonon contribution in the wavevector space,[53] we are able to derive the upper limit of the **q** range (q_{max}) with main contribution to the phonon confinement effect when $\exp(-q^2L_D^2/2\alpha) \rightarrow 1/e$ with L_D of 1 nm, 2 nm, 3 nm, 5 nm and 10 nm and α = 18. The upper limit q_{max} is marked in Fig. 1(e) for each L_D. The phonon branches related to the A_g^2 and B_{2g} modes have intersection or overlapped regions with other phonon branches, which may confuse us to estimate their individual contributions. However, these regions can be defined by q_{max} corresponding to L_D = 1.4 nm for the A_g^2-related branch and L_D = 1.6 nm for the B_{2g}-related branch in Fig. 4(a), as labeled by the two solid circles with Γ as the center, respectively. Thus, for the A_g^2 and B_{2g} modes, the integration over wavevector **q** in eqn (2) can be accomplished within the area circled by the corresponding q_{max} in the Γ–Y–S–X plane.

As seen in Fig. 4, when the 2D phonon dispersion in the Γ–Y–S–X plane of the BZ is considered, the asymmetric tail of the A_g^1 mode at the higher-frequency side and that of the A_g^2 mode at the lower-frequency side are more evident than the simulated profiles based on only the Γ–X and Γ–Y axes in Fig. 3. This is consistent with the variation trend of the corresponding phonon dispersion. As addressed above, the phonon dispersion of the branches associated with A_g^1 is almost flat along the Γ–Y direction and exhibits a marginal redshift before (Γ–Y)/2, while it shows a quickly escalating trend when it extends to the Γ–X direction. The blueshift of phonon dispersion associated with A_g^1 in the Γ–Y–S–X plane gives rise to its asymmetric tail towards the higher-frequency side. It is also the similar case for the A_g^2 mode. The phonon dispersion associated with A_g^2 is almost flat along Γ–X while it exhibits a downhill to the Γ–Y direction, which leads to its asymmetric tail towards the lower-frequency side. As for B_{2g}, its phonon dispersion shows a slight negative and positive slope along the Γ–X and Γ–Y directions, respectively. Their equal contributions would result in an homogeneous broadening of the B_{2g} mode in NCs while its peak position remains unchanged, as shown in Fig. 4(c).

The experimental results are further simulated by the RWL model based on the integration over wavevector wavevector **q** between 0 and q_{max} in the Γ–Y–S–X plane elongated with contributions from phonons with high VDOS, as shown in Fig. 5. The blue dashed lines are the simulated profiles of the A_g^1, B_{2g} and A_g^2 modes based on the RWL model after considering the contribution from the 2D phonon dispersion curves, the gray dashed lines are the SP peaks originating from high VDOS and the pink dashed lines are the superposition of the two contributions. The relative intensity of the SP peaks to the A_g^1, B_{2g} and A_g^2 modes increases with increasing η_{ion}. When η_{ion} increases to 2×10^{13} cm^{-2} (#4-NC), the intensity of the SP4 peaks has surpassed that of the B_{2g} mode. After considering the contribution from the 2D phonon dispersion curves of the whole BZ zone, the asymmetric broadening tail towards the higher-frequency side of the A_g^1 mode is well reproduced, which is attributed to the significant increase of phonon energy toward the X point. The asymmetric broadening tail towards the lower-frequency side of the A_g^2 mode is also well reproduced due to the sharp decrease of phonon energy from Γ–X to Y–S axes. L_D can be estimated from both the fits: 11 nm (#1-NC), 7 nm (#2-NC), 4.4 nm (#3-NC) and 1.8 nm (#4-NC). The A_g^1-related phonon branch shows a nearly flat dispersion in the Γ–Y direction, thus the larger VDOS along the Γ–Y direction results in a maximum peak of the A_g^1 mode in NCs,

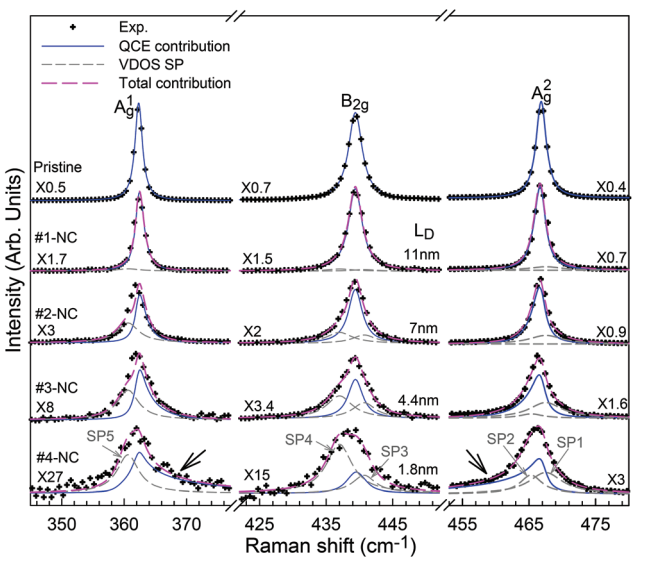

Fig. 5 The experimental data (crosshairs) of the typical Raman modes in pristine BP and BP NC with different estimated domain sizes. The blue dashed lines are the simulated profiles based on the RWL model after considering the contribution of 2D anisotropic phonons from the whole BZ. The gray dash-dotted lines are fits based on the SP peaks in the VDOS. The pink dashed lines are the superposition of the contributions from blue solid and gray dashed lines. The Raman intensity is normalized for comparison.

whose peak position remains almost unchanged with increasing η_{ion}. The branch shows steep and positive dispersion when q approaches the X point from Γ, Y and S points, which contributes to the asymmetric broadening tail towards the higher-frequency side of up to 380 cm^{-1}. Similarly, the nearly flat dispersion of the A_g^2-related phonon branch along the Γ–X results in a maximum peak of the A_g^2 mode in NCs whose peak position remains almost unchanged with increasing η_{ion}, while its steep and positive dispersion from Γ–X to Y–S axes contributes to the asymmetric broadening tail towards the lower-frequency side down to 455 cm^{-1}. These two features cannot be reproduced by the RWL model when only the phonons along Γ–X and Γ–Y axes are considered.

4. Conclusions

In summary, we investigated in detail the evolution of the intensity, line shape and peak position of all the three optical Raman modes of BP NCs with different L_D, which exhibits different behaviors in comparison to other 2D materials, such as TMDs. It is attributed to the pronounced anisotropy of phonon dispersions in pristine BP. In contrast to the crystals with isotropic phonon dispersions along high symmetry directions near Γ, the spectral evolution on L_D cannot be interpreted by the RWL model when only the contributions from phonon dispersions along Γ–X and Γ–Y axes are considered. It is found that the RWL model can be used to well reproduce the line shape and peak position of all the three optical Raman modes in BP NCs after considering the contribution of 2D anisotropic phonon dispersions from the whole BZ, including the asymmetric broadening tails towards the higher-frequency side for the A_g^1 mode and towards the lower-frequency side for the A_g^2 mode. This work confirms that the RWL model can be applicable to understand the phonon confinement effect of the Raman spectra of NCs whose bulk counterpart exhibits anisotropic phonon dispersions.

Conflicts of interest

There are no conflicts to declare.

Acknowledgements

We acknowledge support from the National Key Research and Development Program of China (Grant No. 2016YFA0301204), the National Natural Science Foundation of China (Grant No. 11474277 and 11434010), the Key Research Program of the Chinese Academy of Sciences (Grant No. XDPB06-02, XDPB08-2), and the Beijing Municipal Science and Technology Commission.

References

1 A. Jorio, R. Saito, G. Dresselhaus and M. S. Dresselhaus, *Raman Spectroscopy in Graphene Related Systems*, John Wiley & Sons, 2011.
2 H. Richter, Z. Wang and L. Ley, *Solid State Commun.*, 1981, **39**, 625–629.
3 I. Campbell and P. Fauchet, *Solid State Commun.*, 1986, **58**, 739–741.
4 J. W. Ager, D. K. Veirs and G. M. Rosenblatt, *Phys. Rev. B: Condens. Matter Mater. Phys.*, 1991, **43**, 6491–6499.
5 J. Zi, K. Zhang and X. Xie, *Phys. Rev. B: Condens. Matter Mater. Phys.*, 1997, **55**, 9263–9266.
6 V. Volodin, D. Marin, V. Sachkov, E. Gorokhov, H. Rinnert and M. Vergnat, *J. Exp. Theor. Phys.*, 2014, **118**, 65–71.
7 V. Volodin and V. Sachkov, *J. Exp. Theor. Phys.*, 2013, **116**, 87–94.
8 X. Zhang, X.-F. Qiao, W. Shi, J.-B. Wu, D.-S. Jiang and P.-H. Tan, *Chem. Soc. Rev.*, 2015, **44**, 2757–2785.
9 S. Mignuzzi, A. J. Pollard, N. Bonini, B. Brennan, I. S. Gilmore, M. A. Pimenta, D. Richards and D. Roy, *Phys. Rev. B: Condens. Matter Mater. Phys.*, 2015, **91**, 195411.
10 J.-B. Wu, H. Zhao, Y. Li, D. Ohlberg, W. Shi, W. Wu, H. Wang and P.-H. Tan, *Adv. Opt. Mater.*, 2016, **4**, 756–762.
11 W. Shi, X. Zhang, X. L. Li, X. F. Qiao, J. B. Wu, J. Zhang and P. H. Tan, *Chin. Phys. Lett.*, 2016, **33**, 057801.
12 W. Shi, M. L. Lin, Q. H. Tan, X. F. Qiao, J. Zhang and P. H. Tan, *2D Mater.*, 2016, **3**, 025016.
13 R.-P. Wang, G.-W. Zhou, Y.-L. Liu, S.-H. Pan, H.-Z. Zhang, D.-P. Yu and Z. Zhang, *Phys. Rev. B: Condens. Matter Mater. Phys.*, 2000, **61**, 16827–16832.
14 A. L. Bassi, D. Cattaneo, V. Russo, C. E. Bottani, E. Barborini, T. Mazza, P. Piseri, P. Milani, F. O. Ernst, K. Wegner and S. E. Pratsinis, *J. Appl. Phys.*, 2005, **98**, 074305.
15 G. Faraci, S. Gibilisco, P. Russo, A. R. Pennisi and S. La Rosa, *Phys. Rev. B: Condens. Matter Mater. Phys.*, 2006, **73**, 033307.
16 K.-R. Zhu, M.-S. Zhang, Q. Chen and Z. Yin, *Phys. Lett. A*, 2005, **340**, 220–227.
17 D. Bersani, P. P. Lottici and X.-Z. Ding, *Appl. Phys. Lett.*, 1998, **72**, 73–75.
18 M. Rajalakshmi, A. K. Arora, B. S. Bendre and S. Mahamuni, *J. Appl. Phys.*, 2000, **87**, 2445–2448.
19 K. Roodenko, I. Goldthorpe, P. McIntyre and Y. Chabal, *Phys. Rev. B: Condens. Matter Mater. Phys.*, 2010, **82**, 115210.
20 V. I. Korepanov, H. Witek, H. Okajima, E. Ōsawa and H. O. Hamaguchi, *J. Chem. Phys.*, 2014, **140**, 041107.
21 S. Osswald, V. N. Mochalin, M. Havel, G. Yushin and Y. Gogotsi, *Phys. Rev. B: Condens. Matter Mater. Phys.*, 2009, **80**, 075419.
22 J.-B. Wu, M.-L. Lin, X. Cong, H.-N. Liu and P.-H. Tan, *Chem. Soc. Rev.*, 2018, **47**, 1822–1873.
23 J. Kim, S. S. Baik, S. H. Ryu, Y. Sohn, S. Park, B.-G. Park, J. Denlinger, Y. Yi, H. J. Choi and K. S. Kim, *Science*, 2015, **349**, 723–726.

24 Y. Cai, Q. Ke, G. Zhang, Y. P. Feng, V. B. Shenoy and Y.-W. Zhang, *Adv. Funct. Mater.*, 2015, **25**, 2230–2236.

25 J. Wu, N. Mao, L. Xie, H. Xu and J. Zhang, *Angew. Chem., Int. Ed.*, 2015, **127**, 2396–2399.

26 H. B. Ribeiro, M. A. Pimenta, C. J. S. de Matos, R. L. Moreira, A. S. Rodin, J. D. Zapata, E. A. De Souza and A. H. Castro Neto, *ACS Nano*, 2015, **9**, 4270–4276.

27 J. Kim, J.-U. Lee, J. Lee, H. J. Park, Z. Lee, C. Lee and H. Cheong, *Nanoscale*, 2015, **7**, 18708–18715.

28 X. Ling, S. Huang, E. H. Hasdeo, L. Liang, W. M. Parkin, Y. Tatsumi, A. R. T. Nugraha, A. A. Puretzky, P. M. Das, B. G. Sumpter, D. B. Geohegan, J. Kong, R. Saito, M. Drndic, V. Meunier and M. S. Dresselhaus, *Nano Lett.*, 2016, **16**, 2260–2267.

29 B. S. Elman, M. S. Dresselhaus, G. Dresselhaus, E. W. Maby and H. Mazurek, *Phys. Rev. B: Condens. Matter Mater. Phys.*, 1981, **24**, 1027–1034.

30 P.-H. Tan, Y.-M. Deng, Q. Zhao and W.-C. Cheng, *Appl. Phys. Lett.*, 1999, **74**, 1818–1820.

31 E. H. Martins Ferreira, M. V. O. Moutinho, F. Stavale, M. M. Lucchese, R. B. Capaz, C. A. Achete and A. Jorio, *Phys. Rev. B: Condens. Matter Mater. Phys.*, 2010, **82**, 125429.

32 Q.-Q. Li, X. Zhang, W.-P. Han, Y. Lu, W. Shi, J.-B. Wu and P.-H. Tan, *Carbon*, 2015, **85**, 221–224.

33 A. Favron, F. A. Goudreault, V. Gosselin, J. Groulx, M. Côté, R. Leonelli, J.-F. Germain, A.-L. Phaneuf-L'Heureux, S. Francoeur and R. Martel, *Nano Lett.*, 2018, **18**, 1018–1027.

34 F. Alsaffar, S. Alodan, A. Alrasheed, A. Alhussain, N. Alrubaiq, A. Abbas and M. R. Amer, *Sci. Rep.*, 2017, **7**, 44540.

35 P. Hohenberg and W. Kohn, *Phys. Rev.*, 1964, **136**, B864–B871.

36 G. Kresse and J. Hafner, *Phys. Rev. B: Condens. Matter Mater. Phys.*, 1994, **49**, 14251–14269.

37 W. Kohn and L. J. Sham, *Phys. Rev.*, 1965, **140**, A1133–A1138.

38 P. E. Blöchl, *Phys. Rev. B: Condens. Matter Mater. Phys.*, 1994, **50**, 17953–17979.

39 J. P. Perdew, K. Burke and M. Ernzerhof, *Phys. Rev. Lett.*, 1996, **77**, 3865–3868.

40 G. Kresse and J. Furthmüller, *Phys. Rev. B: Condens. Matter Mater. Phys.*, 1996, **54**, 11169–11186.

41 A. Togo and I. Tanaka, *Scr. Mater.*, 2015, **108**, 1–5.

42 P. W. Bridgman, *J. Am. Chem. Soc.*, 1914, **36**, 1344–1363.

43 C. Kaneta, H. Katayama-Yoshida and A. Morita, *Solid State Commun.*, 1982, **44**, 613–617.

44 J.-W. Jiang, B.-S. Wang and H. S. Park, *J. Phys.: Condens. Matter*, 2016, **28**, 165401.

45 Z. Luo, J. Maassen, Y. Deng, Y. Du, R. P. Garrelts, M. S. Lundstrom, P. D. Ye and X. Xu, *Nat. Commun.*, 2015, **6**, 8572.

46 G. Qin, Q.-B. Yan, Z. Qin, S.-Y. Yue, M. Hu and G. Su, *Phys. Chem. Chem. Phys.*, 2015, **17**, 4854–4858.

47 M. M. Lucchese, F. Stavale, E. H. M. Ferreira, C. Vilani, M. V. O. Moutinho, R. B. Capaz, C. Achete and A. Jorio, *Carbon*, 2010, **48**, 1592–1597.

48 D. J. Late, *ACS Appl. Mater. Interfaces*, 2015, **7**, 5857–5862.

49 W. Lu, H. Nan, J. Hong, Y. Chen, C. Zhu, Z. Liang, X. Ma, Z. Ni, C. Jin and Z. Zhang, *Nano Res.*, 2014, **7**, 853–859.

50 V. Paillard, P. Puech, M. A. Laguna, R. Carles, B. Kohn and F. Huisken, *J. Appl. Phys.*, 1999, **86**, 1921–1924.

51 M. J. Seong, O. I. Mićić, A. J. Nozik, A. Mascarenhas and H. M. Cheong, *Appl. Phys. Lett.*, 2003, **82**, 185–187.

52 A. Molina-Sánchez and L. Wirtz, *Phys. Rev. B: Condens. Matter Mater. Phys.*, 2011, **84**, 155413.

53 A. K. Arora, M. Rajalakshmi, T. R. Ravindran and V. Sivasubramanian, *J. Raman Spectrosc.*, 2007, **38**, 604–617.